

PAPER

Tailoring cavity coupled plasmonic substrates for SERS applications

To cite this article: Jagathpriya L M *et al* 2023 *Nanotechnology* **34** 335501

View the [article online](#) for updates and enhancements.

You may also like

- [Increased atom-cavity coupling and stability using a parabolic ring cavity](#)
Kevin C Cox, David H Meyer, Nathan A Schine *et al.*
- [Narrow-band and highly absorbing fano resonance in a cavity-coupled dielectric metasurface](#)
Jiachen Yu, Qiqige Wulan, Li Xing *et al.*
- [Large gain quantum-limited qubit measurement using a two-mode nonlinear cavity](#)
S Khan, R Vijay, I Siddiqi *et al.*

PRIME
PACIFIC RIM MEETING
ON ELECTROCHEMICAL
AND SOLID STATE SCIENCE

HONOLULU, HI
Oct 6–11, 2024

Abstract submission deadline:
April 12, 2024

Learn more and submit!

Joint Meeting of
The Electrochemical Society
•
The Electrochemical Society of Japan
•
Korea Electrochemical Society

Tailoring cavity coupled plasmonic substrates for SERS applications

Jagathpriya L M , Jayakumar Pillanagrovi  and Shourya Dutta-Gupta 

Materials Science and Metallurgical Engineering, Indian Institute of Technology Hyderabad, Hyderabad, India

E-mail: shourya@msme.iith.ac.in

Received 2 February 2023, revised 10 April 2023

Accepted for publication 12 May 2023

Published 1 June 2023



CrossMark

Abstract

Surface-enhanced Raman spectroscopy (SERS) has been effectively used in biosensing applications due to its high sensitivity and specificity. Enhancing the coupling of light into plasmonic nanostructures can lead to engineered SERS substrates with improved sensitivity and performance. In the current study, we demonstrate a cavity-coupled structure that assists in enhancing the light–matter interaction leading to an improved SERS performance. Using numerical simulations, we demonstrate that the cavity-coupled structures can either enhance or suppress the SERS signal depending on the cavity length and the wavelength of interest. Furthermore, the proposed substrates are fabricated using low-cost large-area techniques. The cavity-coupled plasmonic substrate consists of a layer of gold nanospheres on an indium tin oxide (ITO)-Au-glass substrate. The fabricated substrates exhibit nearly a 9 times improvement in SERS enhancement as compared to the uncoupled substrate. The demonstrated cavity-coupling approach can also be used for enhancing other plasmonic phenomena like plasmonic trapping, plasmon-enhanced catalysis, and nonlinear signal generation.

Supplementary material for this article is available [online](#)

Keywords: plasmonics, cavity-coupling, gold nanoparticles, SERS, sensing

(Some figures may appear in colour only in the online journal)

1. Introduction

Surface-enhanced Raman spectroscopy (SERS)-based sensors are well known for their high sensitivity, specificity, and cost-effectiveness [1–8]. They have been widely used in biosensing applications like cancer diagnosis, detection of biomolecules and pathogens in body fluid and detection of chemicals in food items. In fact, it is possible to even detect a single molecule using SERS spectroscopy [9–13]. For example, Kneipp *et al* demonstrated the detection of single molecule of crystal violet using SERS with colloidal silver nanoparticles [11]. Single-molecule detection was confirmed by observing the change in SERS signal statistics from a Gaussian distribution to a Poisson distribution. The enormous sensitivity of SERS originates from the excitation of plasmons in the structure which lead to enhanced electric fields in the vicinity of the structure and are better known as plasmonic hot-spots. Therefore, it is crucial and vital to tailor-make these

hot-spots for realizing efficient SERS substrates. In this direction, various approaches have been studied. For example, researchers have studied the effect of shape, size, arrangement and materials and their influence on the SERS response [2, 14–17]. In most of these studies, the goal is to achieve the highest SERS enhancement in a reproducible manner. In particular, nanogap formation via different routes enables the realization of the high density of hot-spots [2, 18–20]. Siegfried *et al* have developed a SERS substrate with a reproducible nanogap resonator with strong hot-spots located at the 10 nm gap of nanostructures [21]. Chen *et al* developed a hexagonal closed packed alkanethiolate ligand-regulated silver nanoparticle superlattice with highly reproducible and uniform hot-spots in a large area for the quantitative analysis of crystal violet [12]. Advancements in understanding the effect of various parameters on the plasmon resonance mediated hot-spot generation and next-generation fabrication protocols enable the high-throughput fabrication

of SERS chips [6, 22–36]. Furthermore, most of the demonstrated structures involved various lithography steps (like electron beam lithography, focused ion beam lithography etc) leading to the limited range of the fabricated structures [37–42]. Even though low-cost fabrication techniques based on nanosphere lithography, and laser interference lithography have been reported, they offer poor control over the shape of the plasmonic structure [43, 44]. However, it is possible to combine the advantages of top-down (thin film deposition) and bottom-up (chemical synthesis of nanoparticles) approaches to realize low-cost high-fidelity SERS substrates [45, 46]. For example, Mubeen *et al* have established a SERS substrate with nanoparticle over mirror configuration by coupling a uniform oxide layer deposited using atomic layer deposition (ALD) and dip-coated nanoparticles by means of polymer-based surface functionalization [47].

One of the limiting factors for efficient SERS substrates is the presence of high scattering losses in plasmonic structures leading to the utilization of only a part of incident light intensity for hot-spot generation. In principle, it should be possible to improve plasmonic hot-spots by increasing the proportion of light that is absorbed by the structure. Cesario *et al* have validated a structure for controlling the scattering of incident light by coupling the plasmonic nanoparticles with a metallic mirror separated using a dielectric cavity [48]. It has been demonstrated that, excitation and coupling of localized surface plasmon supported by the nanoparticle and propagating surface plasmon supported by the film result in a multiple resonance response [43, 49, 50]. Various groups have investigated the effect of enhancing the absorption by these cavity-coupled structures for realizing plasmonic perfect absorbers [38, 43, 44, 49–52]. Broadly two different approaches are employed for realizing perfect absorbers. In the first approach, a very small cavity (typically less than 50 nm) is used between the plasmonic nanostructure and a metallic (reflective) layer to induce the formation of dark modes. These modes typically lead to the suppression of reflected intensity thereby increasing the absorption of the structure. However, in this approach, the hot-spot is localized between the metallic structure and the metallic film, making it a challenge to access it for various applications [42, 49, 53, 54]. Leveque *et al* mathematically analyzed the effect of cavity length and the permittivity of the cavity in resonance wavelength [53]. It was shown that the resonance position could be tuned by changing the cavity length. Nevertheless, the hot-spot was located in the photonic cavity, and only a part of it could be accessed. Chu *et al* developed a cavity-coupled structure with double resonance at the excitation wavelength and stokes wavelength of benzenethiol [55]. Even in this structure the near-field enhancement was concentrated inside the cavity. In the second approach, researchers have used larger cavities (with thicknesses comparable to wavelength) for realizing perfect absorbers. In this case, the destructive interference between the reflected waves from various interfaces leads to the perfect absorption of light. The plasmonic structure and cavity length can be tuned to control the net absorption in this structure. Here, hot-spots are available in the vicinity of plasmonic nanoparticles, which

can be accessed easily. Bahramipناه *et al* demonstrated such a perfect absorber using gold nano disks coupled with microcavity with improved sensitivity for refractive index sensing [38]. The coupling of the plasmonic resonators to the photonic cavity resulted in a narrower linewidth which improved the figure of merit. Furthermore, they tuned the length of the cavity for tuning the phase difference between the reflected light to achieve perfect absorption to realize maximum utilization of light for hot-spot generation. In this structure, the analyte was placed inside the cavity resulting in superior interaction between the hot-spots and analyte leading to improved performance.

In the current study, we investigate cavity-coupled plasmonic nanostructures using both numerical and experimental tools. First, we demonstrate the influence of cavity length and other structural parameters on the optical far-field and the near-field response. We compare the response of the cavity-coupled substrate with an uncoupled substrate (bare structure without a mirror layer) to demonstrate the potential improvements due to cavity-coupling. Subsequently, we develop a cost-effective fabrication protocol for the enhanced absorption structure by combining both top-down (sputtering) and bottom-up (chemical synthesis and nanoparticle assembly) approaches. Here, the role of cavity length on the optical and SERS response of cavity-coupled structures has been investigated.

2. Methods

2.1. Materials

Hydrogen tetrachloroaurate (III) hydrate (HAuCl_4 , $\geq 99.9\%$, $393.83 \text{ g mol}^{-1}$), trisodium citrate dehydrate ($\text{Na}_3\text{C}_6\text{H}_5\text{O}_7$, 294.1 g mol^{-1}), silver nitrate (AgNO_3 , $\geq 99.0\%$, $169.87 \text{ g mol}^{-1}$), poly (allylamine hydrochloride) (PAH) (average M.W. = 50 000) and poly (4-styrene sulfonic acid) (PSS) (average M.W. = 75 000; 18 wt% in water) were purchased from Sigma-Aldrich. Sodium chloride (NaCl , 99.9%, 58.44 g mol^{-1} , extra pure A.R.) was purchased from Sisco Research Laboratories Pvt. Ltd 4-Mercaptobenzoic acid (MBA) ($\text{C}_7\text{H}_6\text{O}_2\text{S}$, $>95.0\%$, $154.18 \text{ g mol}^{-1}$) was purchased from Tokyo Chemical Industry. All the reagents were used in the received condition. DI water with a conductivity of $0.067 \mu\text{S cm}^{-1}$ was used for all the reactions. Gold target (99.99%) was purchased from Ted Pella, Inc, and ITO target (99.99%) was purchased from Testbourne Ltd.

2.2. Numerical simulations

The optical response of the cavity-coupled plasmonic substrate (CCP substrate) was calculated using the finite element method software COMSOL Multiphysics using the electromagnetic wave module. The geometry consisted of a gold nanosphere (AuNS) (with diameter, $d = 40 \text{ nm}$) placed on top of a multilayer consisting of an ITO layer (with thickness t), an Au layer (with thickness t_{Au} of 40 nm) and a glass substrate (refractive index of 1.5). The permittivity of gold was

taken from the data of Johnson and Christy [56]. The refractive index of ITO was fixed at 1.8 [57]. The AuNS was immersed in an air medium (refractive index of 1). The structure had a periodicity of P_x and P_y in the x - and y -directions, respectively. In all the simulations, the structure was illuminated using an x -polarized plane wave propagating in the z direction. The response of CCP substrate with varying angles of incidence was calculated using TE polarized light with varying angle of incidence from 0° to 60° and by employing periodic Floquet boundary conditions in the x - and y -directions.

2.3. AuNS synthesis

AuNS were synthesized using citrate-based reduction of HAuCl_4 using the protocol presented by Xia *et al* [58]. Briefly, a premix solution consisting of 250 μL HAuCl_4 (1 wt%), 170 μL trisodium citrate (1 wt%), 21.25 μL AgNO_3 (0.1 wt%), and 808.75 μL of DI water was prepared. After 4 min incubation, the premix solution was introduced into boiling water (23.75 ml) which was stirred at 1500 rpm. After the addition of the premix solution, the color of the solution changed from colorless to dark violet to wine red color indicating the formation of AuNS. The solution was refluxed for 30 min. The absorbance spectrum of the prepared AuNS was measured using an ultraviolet–visible (UV–vis) spectrometer (Perkin Elmer - Lambda 365). The size analysis of AuNS was carried out using a transmission electron microscope (TEM) (JEOL-JEM2100 operated at 200 KV).

2.4. Fabrication of CCP substrates

An ITO adhesion layer was deposited using DC magnetron sputtering (Excel instruments-DC magnetron sputtering system) over a cleaned glass slide with a deposition pressure of 3.2×10^{-2} mbar with a 10:1 ratio of Ar and O_2 for 1 min leading to a thickness of around 20 nm. Subsequently, an Au mirror of 40 nm thickness was deposited using a benchtop sputtering machine (Quorum-Q150RS Plus) with a deposition current of 40 mA for 2 min. Finally, an ITO thin film with varying thickness was deposited using DC magnetron sputtering over the Au mirror in a plasma of Ar and O_2 in a 10:1 ratio at a deposition pressure of 3.2×10^{-2} mbar. The base pressure was kept fixed at 5.5×10^{-6} mbar for all the depositions. The thickness of the film was varied by controlling the deposition time. The multi-layer structure (Glass-Au-ITO) was coated with alternating polyelectrolyte (PE) layers of PAH and PSS [17, 59]. A total of 5 PE layers (PAH-PSS-PAH-PSS-PAH) were deposited by immersion. In each step, the substrate was immersed in the PE solution (3 mm concentration) for 10 min. In between each PE coating, the substrate was thoroughly washed and immersed in DI water for 1 min and 1 M NaCl solution for 30 s. After PE coating, the substrate was immersed in the prepared AuNS solution for 4 h. for the adhesion of negatively charged AuNS onto the positively charged PE-coated substrate. The fabricated substrates were imaged using a FESEM (JEOL JIB4700F). Finally, for SERS analysis, the substrates were incubated in

100 μM MBA solution for 1 h. After the incubation, the substrates were thoroughly washed with DI water and dried in the air before the measurements.

2.5. Reflection and transmission spectroscopy

The optical response (reflection (R) and transmission (T)) was measured using a homemade optical setup. A broadband halogen light source was used to illuminate the samples for all the measurements. For measuring the transmission spectrum, the light was incident on the sample placed on an inverted optical microscope (Nikon Ti2U) at the near-normal incidence and the transmitted light was collected using a 20X objective (0.45 NA). Subsequently, the light was analyzed using a spectrometer (Andor Kymera 328i with Newton 920 CCD camera). The transmitted intensity was normalized to the light intensity through the air to acquire the transmission spectrum. For the reflection spectrum, the light was incident on the sample through the air using a 20X objective and the same objective was used to collect the reflected light. Subsequently, the reflected light was analyzed using the spectrometer. The reflected intensity was normalized to the light intensity from a silver mirror to obtain the reflection spectrum. In all the measurements, 150 lines mm^{-1} grating and a slit width of 10 μm were used. The absorption (A) of the sample was calculated using the following equation: $A = 1 - R - T$, where R and T are the normalized reflection and transmission intensities, respectively.

2.6. Numerical simulation of nonregular arrangement of AuNS substrates

Numerical simulation of a substrate with the nonregular arrangement of AuNS was carried out using finite element software COMSOL multiphysics. The distribution and size of nanoparticles was extracted from the SEM images of fabricated CCP substrates using ImageJ software. Nine different locations (each with an area of 300 nm \times 300 nm) was simulated for CCP substrates with cavity lengths of 200 nm, 222 nm and 244 nm and bare substrate. In each of these cases, P_x and P_y were chosen as 300 nm. The response of a regular arrangement of AuNS based CCP substrate with the identical particle density as that of the nonregular CCP substrate was also simulated as a control. In this case, the periodicity in x and y was fixed based on the particle density and is given in table S1.

2.7. SERS analysis

The Raman spectrum of the samples (after incubation with MBA) was measured using a homemade optical setup. We used MBA as a Raman reporter molecule for evaluating the SERS efficiency of the fabricated structures. Recall that MBA exhibits two prominent Raman peaks at 1573 cm^{-1} and 1070 cm^{-1} , respectively [17]. A 594 nm laser (Coherent Obis 594LX) at a power of 1 mW was used to illuminate the sample through a 60X (NA 0.7) objective in the reflection configuration. Laser spot size (diameter at $1/e^2$ of the maximum intensity) was estimated as 18.1 μm by ImageJ analysis

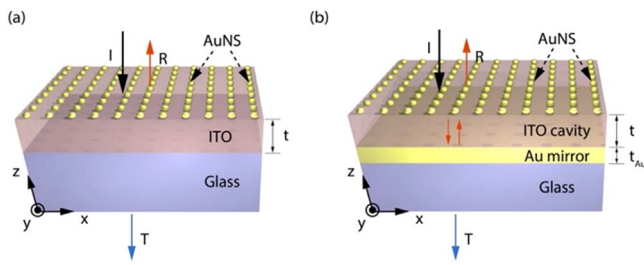


Figure 1. Cavity-coupled plasmonic substrate. Schematic illustrating the interaction of (a) bare substrate and (b) CCP substrate consisting of the gold mirror, ITO cavity and layer of AuNS with incident radiation (I) and its response.

using the image of the laser spot. The Raman scattering was collected using the same objective and analyzed using the spectrometer (Andor Kymera 328i with Newton 920 CCD camera). For all the Raman measurements, we used a grating with $600 \text{ lines mm}^{-1}$ and a slit width of $300 \mu\text{m}$. The spectra were acquired with 3 accumulations and an exposure time of 10 s each.

3. Results and discussion

3.1. Absorption control using CCP substrates

Figure 1(a) shows a conventional SERS substrate (referred to as a bare substrate in subsequent sections) consisting of a layer of AuNS placed on top of a dielectric substrate (ITO-glass). However, the CCP substrate (figure 1(b)) consists of a layer of AuNS placed on top of an optical cavity. In the CCP substrate, the optical cavity is made by ITO and enclosed by a gold mirror (bottom) and the AuNS layer (top). Unlike the bare substrate where the reflection and transmission intensities are governed by the size, shape and interparticle spacing of AuNS, in case of the CCP substrate along with previously mentioned parameters cavity length, mirror material (Ag, Au), and thickness of mirror determines its optical response [38]. In particular, by controlling the thickness of the ITO layer, it is feasible to control the phase difference between the waves reflected at various interfaces and thereby the net reflection from the structure. When we achieve constructive interference of the waves, we obtain enhanced reflection from the substrate. On the other hand, in the case of destructive interference, we can suppress the reflection from the substrate. Parallely, the Au layer thickness enables us to tune the transmission intensity. Consequently, it is possible to control the reflection and transmission by appropriately tuning the cavity geometry for a fixed AuNS layer. Under specific conditions, it is possible to minimize both reflection and transmission simultaneously, leading to enhancement in the absorption by the structure. In the extreme limit when absorption reaches unity, the structures exhibit the so-called perfect absorption or critical coupling [38, 41].

Figures 2(a) and (b) shows the unit cell of the substrates used for the simulations with a regular arrangement of AuNS. As mentioned, an AuNS of 40 nm diameter is placed on top of a glass-Au-ITO stack with a period of 50 nm. Figures 2(c)–(e)

shows the simulated reflection, transmission, and absorption spectra of the substrates as a function of wavelength for various ITO cavity lengths ranging from 160 to 280 nm. The black curves in figure 2(c) shows the reflection and figure 2(d) shows the transmission of AuNS placed on top of the glass-ITO stack (bare). Note that in the absence of the Au mirror, the reflection spectrum shows a prominent peak at around 530 nm with an intensity of 24%. Correspondingly, in the transmission spectrum, we observe a dip at 520 nm with an intensity of 48%. Consequently, for this structure, the maximum absorption of 28% at 520 nm is observed. For the CCP substrate, the reflection spectrum is strongly dependent on the thickness of the ITO layer. For example, for 160 nm ITO thickness the reflection shows dips at 490 nm and 550 nm. However, for 200 nm ITO thickness, the dips are seen at 500 nm and 610 nm. Furthermore, there is a systematic red shift in the dip occurring at the higher wavelength as the thickness changes from 160 to 240 nm. On further increasing the thickness to 280 nm, we observe that a dip is again observed close to 470 nm and 530 nm. This trend is due to the systematic change in the phase difference between the reflected waves and the wavelength at which the destructive interference occurs is higher for larger ITO thicknesses. As destructive interference occurs due to any phase difference of the reflected waves of odd multiples of π , it is possible to obtain destructive interference for smaller wavelengths like for ITO thickness of 280 nm. The observed trend in resonance wavelength shift also agrees well with that observed for Fabry–Perot cavities with varying cavity lengths [38]. Analogously, in the transmission spectrum for the CCP substrate, we observe a progressive redshift of the peak from 580 to 640 nm as the thickness is increased from 160 to 220 nm. The 280 nm ITO thickness shows a peak at 550 nm and agrees well with the resonance observed from the reflection spectrum. Due to the presence of the Au mirror, the maximum transmission intensity for various ITO thicknesses does not exceed 25%. In order to understand the nature of the modes supported by the structure, we have plotted the electric field components on various planes as shown in figure S2 and figure S3. Figure S2 shows the electric components at 594 nm (corresponding to the laser wavelength) on the XY, YZ and ZX planes. Due to incidence of x -polarized plane waves, the x -component of the electric field is the strongest. Furthermore, the field distribution indicates a dipolar mode being excited at the low-energy resonance. Figure S3 shows the electric field intensity for the bare substrate and the CCP substrate. From the near-field plots it is evident that the near-field is enhanced due to cavity coupling. Figure 2(e) shows the absorption spectrum for various ITO thicknesses as a function of wavelength. From an application point of view, we have analyzed absorption intensities at laser wavelength (λ_L) at 594 nm, 1st stokes line of MBA (λ_{S1}) at 634.32 nm and 2nd stokes line of MBA (λ_{S2}) at 655.22 nm (vertical dotted lines). The uncoupled substrate exhibits an absorption intensity of 5% at the laser wavelength. CCP substrate of 180 nm ITO thickness is having highest absorption of 49% at laser wavelength compared to all other CCP substrates. As compared to the uncoupled structure the CCP substrate with ITO thickness of 180 nm has around 10 times improvement in absorption at the laser wavelength.

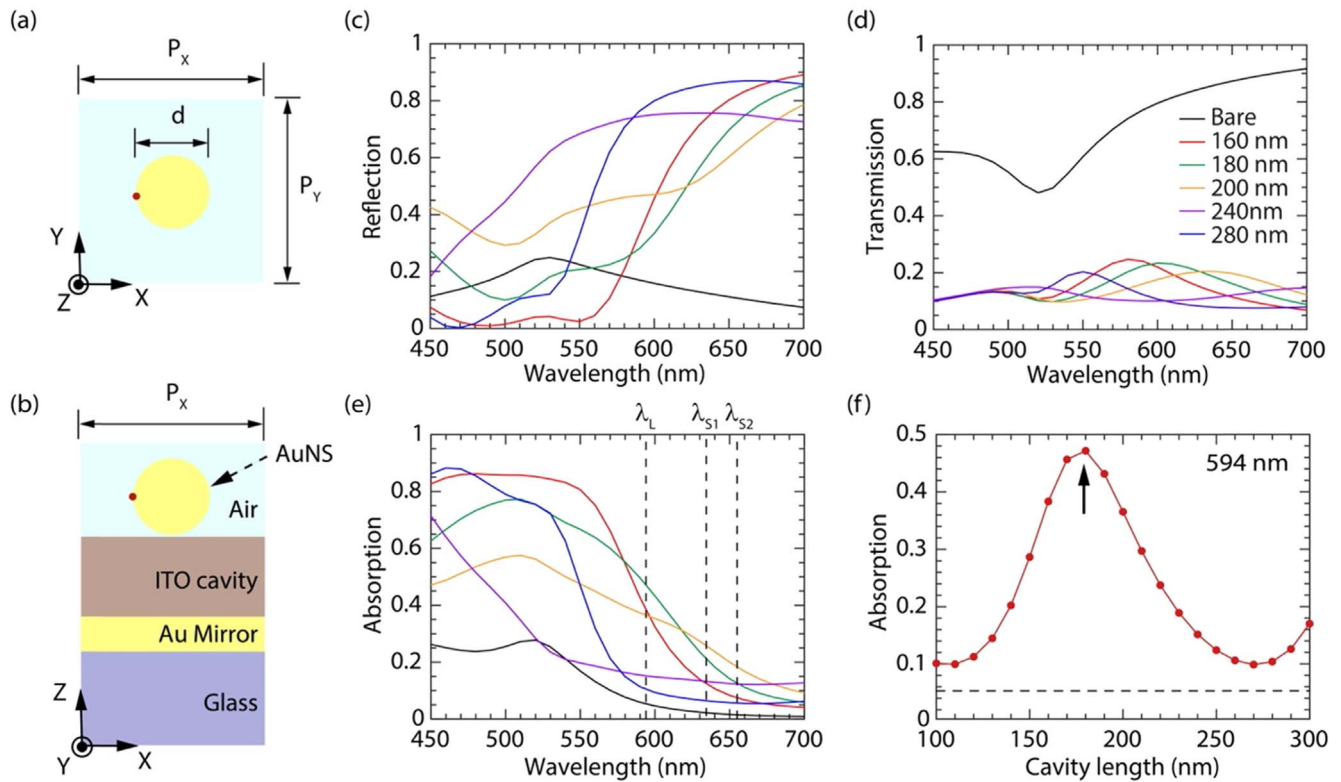


Figure 2. Simulated optical response of the CCP substrates. The unit cell of the structure used for simulation (a) top-view (b) side-view and the optical response from the substrates with a period of 50 nm (c) reflection, (d) transmission and (e) absorption as a function of wavelength for different ITO cavity lengths. The black line corresponds to the response of the uncoupled substrate (bare substrate). Vertical dotted lines λ_L , λ_{S1} and λ_{S2} correspond to the absorption by the structures at the laser wavelength, first stokes and second stokes line respectively (f) Absorption as a function of the cavity length (t) at the laser wavelength (594 nm (λ_L)) by the cavity coupled substrate (red line) and uncoupled substrate (black dotted line). The black arrow mark indicates the cavity length of the substrate with the highest absorption.

However, a substrate with ITO thickness of 200 nm has the highest absorption of 26% and 20% at 1st and 2nd MBA stokes lines respectively. Whereas uncoupled structure has an absorption of 2% at MBA stokes lines. Hence, the absorption of the substrate can be modified by controlling the ITO thicknesses. Figure 2(f) shows the absorption by the CCP substrate as a function of cavity length from 100 to 300 nm (red line) and the dashed line is the corresponding response from the uncoupled substrate at the laser wavelength. Here with an increase in ITO thickness, absorption also increases and reaches absorption maxima for 180 nm cavity length (indicated by arrow) which is due to the destructive interference of reflected waves. Further increase in ITO thickness leads to the reduction in absorption due to constructive interference of reflected waves. Similarly, figure S1 shows the absorption spectra of the CCP substrates at 1st and 2nd stokes lines of MBA as a function of the cavity length. 200 nm cavity structure gives the highest absorption to the 1st stokes line of MBA, whereas 210 nm cavity structure gives the highest absorption to the 2nd stokes line of MBA. Dashed lines show the response of the uncoupled structure at 1st (red) and 2nd (black) stokes lines. Compared to uncoupled structures, CCP substrates have above 10 times enhancement in absorption at MBA stokes lines. As the current substrates have been proposed as SERS substrates, it is important to understand the influence of incidence and collection angle on the optical response of the CCP

substrates. Figure S4 shows the colormap of reflection by the CCP substrate (with a cavity length of 180 nm) for a TE polarised incident light with varying angle of incidence from 0° to 60° . As the incidence angle is increased, a gradual blue shift of the low-energy resonance is observed. Additionally, the reflection dip becomes more prominent for larger incidence angles with the minimum reflectivity changing from around 0.25 to 0.04.

Additionally, to understand the influence of the periodicity of the structure, we have analyzed the response of a structure with a period of 100 nm (see figure S5). Figures S5(a)–S5(c) shows the reflection, transmission, and absorption spectra of a CCP substrate composed of 40 nm AuNS placed on an ITO-coated gold mirror layer (40 nm) with a period of 100 nm. In figure S5(a) reflection is increasing as the ITO thickness increases. The structures have a similar transmission with a redshift in its peak as ITO thickness increases (figure S5(b)), with a broader response compared to the structure with a period of 50 nm. For 1st and 2nd stokes wavelengths of MBA molecule, a cavity length of 240 nm shows maximum absorption (figure S5(c)). Figure S5(d) shows the absorption spectra of the structure with varying ITO cavity lengths from 100 to 300 nm at laser wavelength (red line) and the dashed line is the performance of the uncoupled substrate. Here with an increase in cavity length absorption also increases and after absorption maxima at

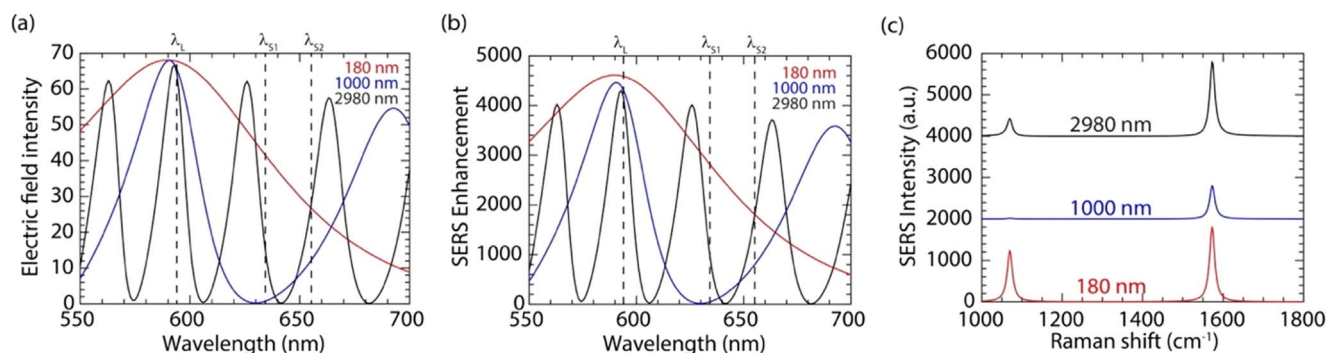


Figure 3. Effect of cavity length on the SERS performance of the CCP substrates. (a) Electric field enhancement as a function of wavelength with varying ITO cavity lengths of 180 nm, 1000 nm and 2800 nm respectively (b) SERS enhancement as a function of wavelength with varying ITO cavity length. Vertical lines λ_L , λ_{S1} and λ_{S2} correspond to the response of the structures at the laser wavelength, first stokes and second stokes line respectively. (c) Simulated SERS spectra of MBA with varying ITO cavity lengths. Each spectrum is shifted by 2000 units along the y-axis.

210 nm (black arrow), we can see the reduction in absorption with further increase in cavity length as in coupled structure with a period of 50 nm. Analogous to the 50 nm period, the 100 nm periodicity structure also shows similar trends albeit the maximum absorption at laser wavelength occurs for a cavity length of 210 nm. However, the absorption is enhanced by a factor of 37 due to cavity-coupling. Nonetheless, for a cavity of 180 nm compared to a 100 nm period CCP substrate, a 50 nm period substrate showed about two times increment in absorption.

3.2. Near field response of CCP substrates

The effect of ITO thickness on the SERS performance of the substrate is studied by calculating the electric field on the surface of the particle in the direction of polarization (along the x -axis) shown in figures 2(a) and (b) (red dot). Here we have considered ITO thicknesses that are less than, comparable to, and greater than wavelengths of interest 180 nm, 1000 nm, and 2980 nm respectively. Figure 3(a) shows the electric field intensity on the surface of the AuNS situated in the CCP substrate. Black dotted vertical lines λ_L , λ_{S1} and λ_{S2} correspond to the electric field enhancement of the structures at the laser wavelength, 1st stokes, and 2nd stokes lines of MBA respectively. The 180 nm substrate has electric field intensity maxima of 68 at 590 nm. As we increase the ITO thickness to 1000 nm observed dual maxima and single minima in the wavelength range of 550–700 nm. As the thickness is increased further to 2980 nm multiple minima and maxima emerged. SERS enhancement provided by these three substrates to the 2nd stoke line of MBA is calculated at a point on the surface of AuNS in the direction of polarization (x -axis) using the normalized electric field at laser wavelength E_L and at stokes line E_S using the equation, SERS enhancement = $|E_L|^2|E_S|^2$. SERS enhancement also shows a similar trend as field intensity, 180 nm cavity substrates provide non-zero enhancement for the MBA stokes line in the wavelength range of 550–700 nm. However, 1000 nm and 2980 nm cavity-length structures show multiple maxima and minima within the wavelength range (figure 3(b)). Furthermore, the

calculated SERS efficiency of the CCP substrate with three cavity lengths, 180 nm, 1000 nm and 2980 nm for MBA molecule, is shown in figure 3(c). Here, we have calculated the SERS enhancement by multiplying the intensity of the simulated MBA spectrum (figure S6) with the SERS enhancement provided by the substrates with varying ITO thicknesses. The stokes positions of MBA, 634.32 nm and 655.22 nm, were obtained from previous reports, and the peak ratio of 0.4 was obtained from the Raman spectrum of MBA collected experimentally using an uncoupled substrate [17]. Compared to the substrate with ITO thickness of 1000 nm and 2980 nm, 180 nm exhibits peak enhancement for both the stokes lines. For the 1000 nm cavity substrate, the 1st stokes line is diminished since the 1st stoke line of MBA coincides with the minima in the SERS intensity. A structure with 2980 nm provides a higher enhancement for the 2nd stokes line than the 1st stokes line. From this analysis, it is evident that in the case of structures with large cavity lengths (exhibiting multiple maxima and minima in the enhancement spectrum), there is a possibility of significant alteration to the Raman spectrum. Such a significant modification was observed in the case of the ITO cavity length of 1000 nm (figure 3(c)). When employing such SERS substrates for sensing applications, this kind of alteration in the spectrum can lead to the misidentification of the molecules.

3.3. Optical measurements of CCP substrates

The CCP substrates are developed by the assembly of chemically synthesized AuNS on PE functionalized sputter-coated glass-ITO-Au-ITO stack, as shown in the schematic (figure 4(a)). An ITO layer below the Au mirror serves as an adhesion layer [60]. The substrates are developed with 40 nm Au mirror, varying ITO cavity length of 200 nm, 222 nm, 244 nm, 261 nm and 280 nm and decorated with synthesized AuNS. The narrow absorbance peak at 524 nm from the UV–Visible spectrum of the particle shows uniform particle distribution (figure S7(a)). Particle size and morphology have been studied using TEM (figure S7(b)), and particles are having an average diameter of 34 ± 2 nm (figure S7(c)).

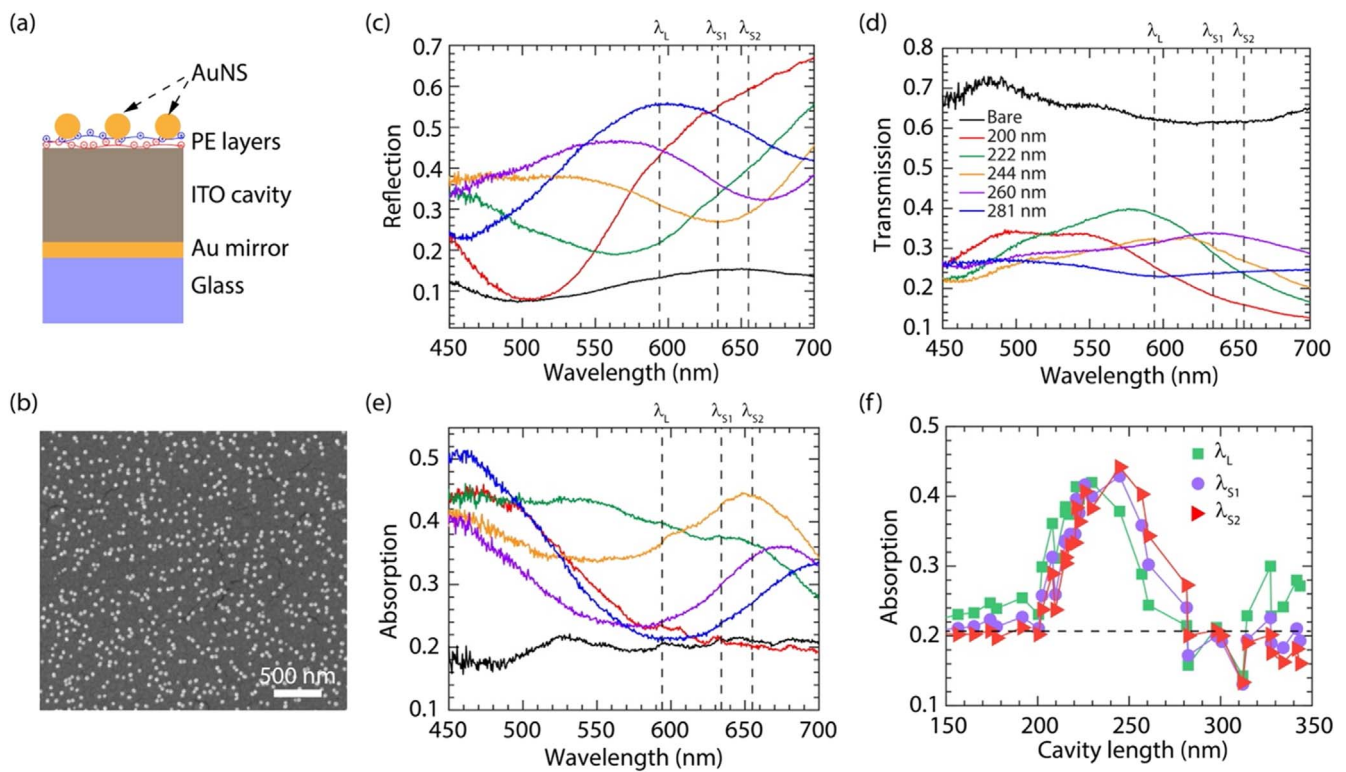


Figure 4. Experimental characterization of CCP substrates. (a) Schematic of the fabricated CCP substrate. (b) SEM of the fabricated CCP substrate. (c) Reflection spectra, (d) transmission spectra and (e) absorption spectra of multilayer substrates as a function of wavelength for varying ITO cavity lengths. Vertical lines λ_L , λ_{S1} and λ_{S2} correspond to the optical response by the structures at the laser wavelength, first stokes and second MBA stokes line respectively. (f) Absorption of multilayer substrates as a function of ITO cavity length at the laser wavelength, first stokes and second stokes lines of MBA respectively. The black dotted line corresponds to the absorption by the uncoupled substrate at the laser wavelength.

Transparent ITO cavities are deposited in the presence of argon and oxygen with a ratio of 10:1 [61]. The top morphology of the ITO cavity decorated with AuNS is shown in figure 4(b). Figure S7(d) shows particle density with respect to cavity length, calculated from SEM images of CCP substrate using the ImageJ software. Here structures with varying cavity lengths from 150 to 350 nm are having an average of 70 ± 3 particles μm^{-2} .

Figures 4(c)–(e) shows the reflection, transmission, and absorption of the CCP substrate as a function of wavelength with varying cavity lengths. The black curves in figure 4(c) shows the reflection and figure 4(d) shows the transmission of AuNS placed on top of the glass-ITO stack (bare). This substrate without a mirror layer has a reflection of around 10% and transmission of around 70%, resulting in absorption of around 20%. However, with the introduction of an Au mirror to the substrate the optical response varies significantly due to the formation of the photonic cavity. A substrate with a cavity length of 244 nm shows reflection minima at stokes wavelengths whereas the one at 220 nm shows minima at laser wavelength (figure 4(c)). Similarly, transmission by the structure with 222 nm cavity is about 30% at stokes wavelengths, while it is about 40% at the laser wavelength. The CCP substrate with 244 nm cavity length has transmission around 30% in both laser and stokes wavelengths (figure 4(d)). As a result, the cavity length of 244 nm has an absorption of about 41% and 45% at 1st and 2nd stokes lines

of MBA respectively (figure 4(e)). A structure with a cavity length of 222 nm has about 40% absorption at laser wavelength. Absorption spectra with respect to cavity lengths at laser wavelength (green square) and stokes wavelengths (violet circle and red triangle) are shown in figure 4(f). For stokes wavelengths (λ_{S1} and λ_{S2}) absorption increases with an increase in cavity length from 150 nm and reaches maxima at 244 nm, due to the destructive interference of reflected lights and reduces with a further increase in cavity length to 340 nm. Even though the laser wavelength follows the same trend, it has absorption maxima at 222 nm cavity length. The black dotted line shows the absorption by the uncoupled substrate. This demonstrates the cavity-length mediated control of the absorption by the CCP substrate.

3.4. Influence of nonregular arrangement of AuNS in CCP substrate

Self-assembly of AuNS over PE functionalized ITO cavity results in a nonregular (NR) arrangement of AuNS (figure 4(b)). Therefore, in order to understand the influence of the nonregular arrangement of AuNS on CCP substrate, we simulate realistic CCP substrates using the finite element method. The diameter and particle distribution of AuNS are extracted using ImageJ software from the SEM images of the fabricated substrates. Figure 5 shows the far-field and near-field response of bare substrate and CCP substrates with

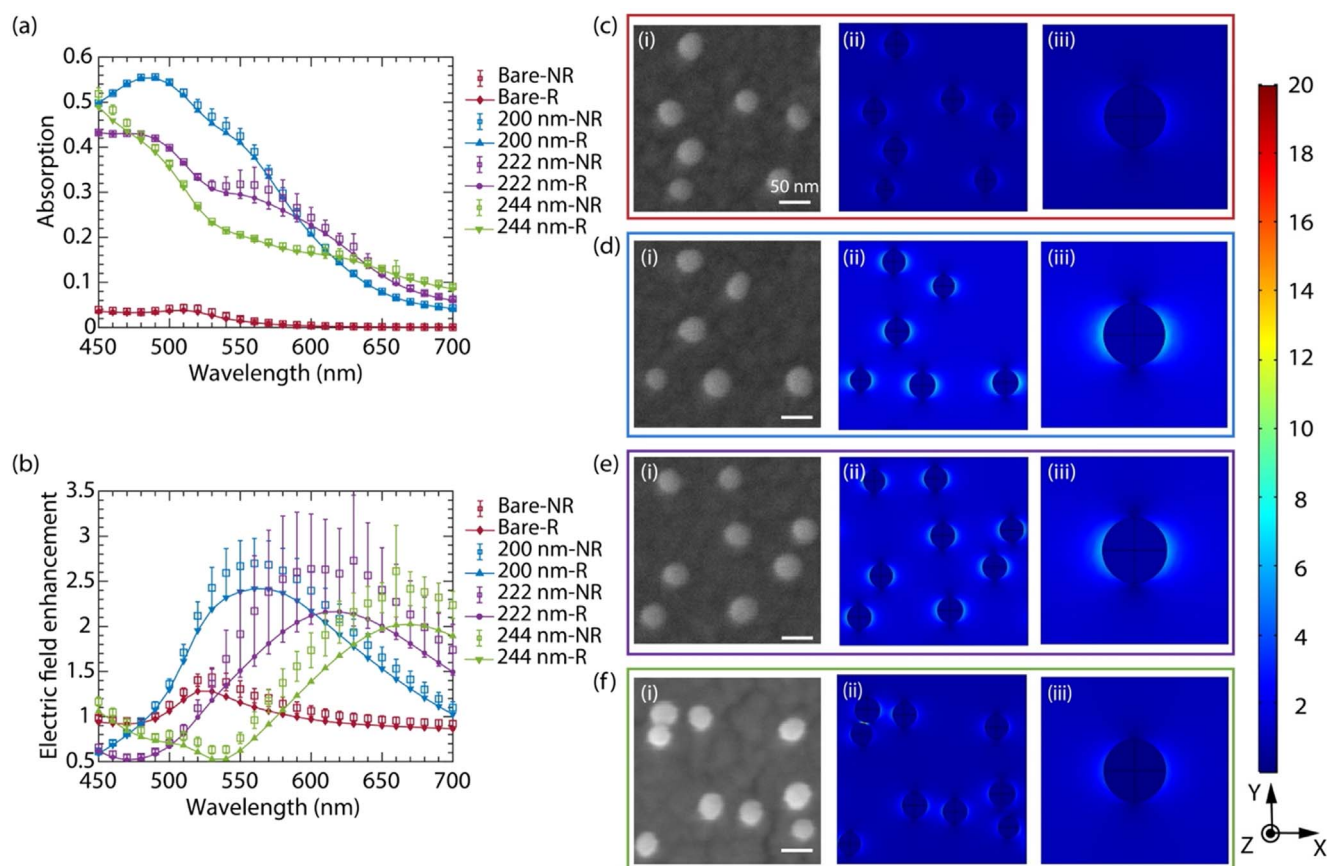


Figure 5. Simulated response of CCP substrate with regular and nonregular arrangement of AuNS. (a) Absorption, (b) electric field enhancement as a function of wavelength for CCP substrates (nonregular and regular arrangement of AuNS) with varying cavity lengths. The CCP substrate with nonregular and regular arrangement of AuNS have identical particle density. (c)–(f) The representative SEM images (shown in (i)), corresponding near field enhancement (shown in (ii)), and near field enhancement of CCP substrates with regular arrangement (shown in (iii)) of bare substrate (c) and CCPS substrates with cavity lengths of 200 nm (d), 222 nm (e), and 244 nm (f). A period of 300 nm is used to simulate the response of the substrate with nonregular arrangement of AuNS. The period used for simulation of CCP substrate with regular AuNS arrangement is given in table S1. The wavelength in (c)–(f) is fixed at 590 nm.

varying cavity lengths of 200 nm, 222 nm, and 244 nm for the nonregular (NR) arrangement of AuNS. The response of CCP structure with nonregular (NR) and regular (R) arrangement of AuNS is compared to exhibit the influence of ordering. In these simulations, the period for the regular arrays was fixed such that the particle densities in each case are identical and the details are presented in table S1. For each case, the nonregular and regular arrangements show similar trends in absorption and electric field enhancement, as depicted in figure 5. However, substrates with a nonregular arrangement of AuNS exhibit higher absorption and field enhancement as compared to the regular arrangement based CCP structure (figure 5(a)). This demonstrates that the arrangement of AuNS on the CCP substrate has minimal influence on the modal character of the CCP structure but influences the final obtained enhancement factor. Figures 5(c)–(f) and figures S8–S11 show the near-field maps of both nonregular and regular structures which clearly shows the dipolar fields around the AuNS in both these cases. However, the variation in nearfield values at a given wavelength is due to the hot-spots formed in some of the cases due to very small inter-particle gaps (SEM images in figures 5(c(i)–f(i)) and figures S8(i)–S11(i)).

3.5. SERS response of the CCP substrates

We have studied the SERS response of CCP substrates using MBA, a Raman marker with characteristic peaks at 1063 cm^{-1} and 1573 cm^{-1} . Figure 6(a) shows the SERS spectra of MBA on CCP substrates with varying ITO cavity lengths. It is observed that with varying cavity lengths, SERS intensity also varies. The substrate with an ITO cavity of 244 nm provides a maximum enhancement of 9 times (for 1573 cm^{-1}) compared to the uncoupled structure. Because it has a higher absorption at stokes wavelengths. The CCP substrate with 222 nm cavity length has about 8 times enhancement which has absorption maxima around laser wavelength. So, by tuning the cavity length we can tune the resonance of the CCP substrate to obtain enhanced SERS intensity. Figure 6(b) shows the SERS intensity of MBA by CCP substrates and uncoupled substrate (dashed line) as a function of cavity lengths. In the CCP substrates as the cavity length increases SERS intensity also increases till the cavity length of 244 nm. Further increase in cavity lengths resulted in a decrease in SERS intensity. We demonstrated that the trend observed due to cavity length variations is similar in both numerical and experimental approaches. However, the

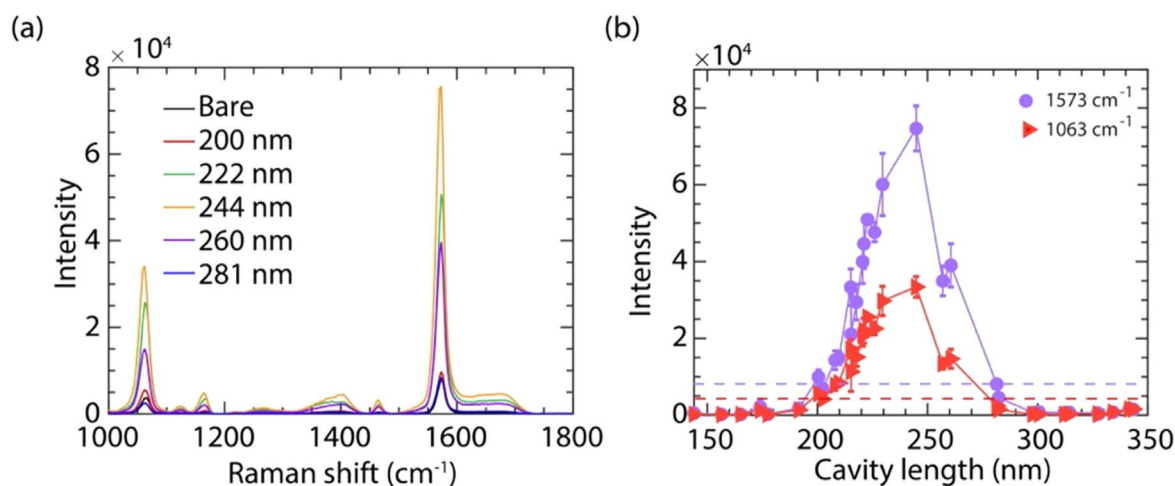


Figure 6. SERS spectra of MBA by CCP substrates. (a) SERS intensity of MBA molecules as a function of Raman shift provided by CCP substrates with varying cavity lengths. (b) SERS intensity of MBA molecules as a function of cavity length for the Stokes lines 1063 cm^{-1} and 1573 cm^{-1} . Dashed lines indicate the corresponding SERS intensity provided by uncoupled substrate.

optimal cavity lengths are different in these two cases. For example, in the numerical simulations the optimal cavity length is 180 nm (figure 2) whereas from the experimental measurements, the optimal cavity length was determined to be 244 nm (figure 4 and figure 6). The difference in the simulations and the experiments can potentially arise from the differences in permittivity (of the various materials), size distribution of the AuNS and experimental measurement geometry used. The proposed method for enhancing the SERS signal is very generic and can be extended for other laser wavelengths and analytes. Various geometrical parameters like the cavity length, AuNS size, interparticle distance and Au thickness can be optimized to achieve the highest possible enhancement factor. Figure S12 shows the ratio of intensities of 1st and 2nd Stokes lines of MBA for CCP substrates (blue solid line) and uncoupled substrates (red dashed line) with respect to different cavity lengths. Here intensity ratio shows variation with varying ITO thicknesses. We observed that the coupled substrates show improved SERS enhancement compared to an uncoupled substrate. Thus the CCP substrate can be exploited for SERS-based biosensing. In order to evaluate the efficiency of the developed SERS substrates we have calculated the limit of detection using the experimentally measured parameters. Using the CCP structure with a cavity length of 244 nm, we have calculated the limit of detection to be 4.5 atto-moles (details in supporting information section S1).

4. Conclusions

In summary, we have developed a SERS substrate based on the cavity-coupling principle using a hybrid-nanofabrication process involving sputtering and nanoparticle assembly. We have studied the influence of various geometrical parameters on the optical response (both near- and far-field). The ITO cavity length can be used to tune the interplay between constructive and destructive interference between the waves

reflected at various interfaces and thereby the net absorption by the structure. Numerically, we demonstrated that the cavity-coupled substrate with a cavity length of 180 nm showed around 10 times enhancement in absorption compared to an uncoupled structure at the laser wavelength. The structures were experimentally fabricated using a combination of sputtering and nanoparticle self-assembly. The experimentally fabricated substrates exhibited a 9 times enhancement in the SERS signal of MBA molecules for a cavity length of 244 nm as compared to an uncoupled substrate. Furthermore, the SERS enhancement was shown to be highly dependent on the cavity length and the SERS signal could either be enhanced or suppressed by an appropriate choice of cavity length. In the future, the developed substrates can also be used for various applications like nonlinear signal enhancement, biosensing, and plasmonic trapping.

Acknowledgments

This work was supported by SERB Ramanujan Grant SB/S2/RJN-126/2017 and DST Nanomission Grant DST/NM/NB/2018/118.




Data availability statement

All data that support the findings of this study are included within the article (and any supplementary files).

Conflict of interest

The authors have no known conflict of interests concerning the publication of this research.

ORCID iDs

Jagathpriya L M  <https://orcid.org/0009-0002-3736-306X>
 Jayakumar Pillanagrovi  <https://orcid.org/0000-0001-8373-4891>
 Shourya Dutta-Gupta  <https://orcid.org/0000-0001-5680-3847>

References

- [1] Wang M, Cao X, Lu W, Tao L, Zhao H, Wang Y, Guo M, Dong J and Qian W 2014 Surface-enhanced Raman spectroscopic detection and differentiation of lung cancer cell lines (A549, H1229) and normal cell line (AT II) based on gold nanostar substrates *RSC Adv.* **4** 64225–34
- [2] Mercadal P A, Encina E R and Coronado E A 2019 Colloidal SERS substrate for the ultrasensitive detection of biotinylated antibodies based on near-field gradient within the Gap of a nanoparticle dimers *J. Phys. Chem. C* **123** 23577–85
- [3] Zhong L-B, Yin J, Zheng Y-M, Liu Q, Cheng X-X and Luo F-H 2014 Self-assembly of au nanoparticles on pmma template as flexible, transparent, and highly active SERS substrates *Anal. Chem.* **86** 6262–7
- [4] Lane L A, Qian X and Nie S 2015 SERS nanoparticles in medicine: from label-free detection to spectroscopic tagging *Chem. Rev.* **115** 10489–529
- [5] Li X, Soler M, Szydzik C, Khoshmanesh K, Schmidt J, Coukos G, Mitchell A and Altug H 2018 Label-free optofluidic nanobiosensor enables real-time analysis of single-cell cytokine secretion *Small* **14** 1800698
- [6] Lee T, Kwon S, Choi H-J, Lim H and Lee J 2021 Highly sensitive and reliable microrna detection with a recyclable microfluidic device and an easily assembled SERS substrate *ACS Omega* **6** 19656–64
- [7] Cho H, Kumar S, Yang D, Vaidyanathan S, Woo K, Garcia I, Shue H J, Yoon Y, Ferreri K and Choo H 2018 Surface-enhanced raman spectroscopy-based label-free insulin detection at physiological concentrations for analysis of islet performance *ACS Sens.* **3** 65–71
- [8] Wang J, Koo K M, Wee E J H, Wang Y and Trau M 2017 A nanoplasmonic label-free surface-enhanced Raman scattering strategy for non-invasive cancer genetic subtyping in patient samples *Nanoscale* **9** 3496–503
- [9] Doering W E and Nie S 2002 Single-molecule and single-nanoparticle sers: examining the roles of surface active sites and chemical enhancement *J. Phys. Chem. B* **106** 311–7
- [10] Prinz J, Heck C, Ellerik L, Merk V and Bald I 2016 DNA origami based Au–Ag-core–shell nanoparticle dimers with single-molecule SERS sensitivity *Nanoscale* **8** 5612–20
- [11] Kneipp K, Wang Y, Kneipp H, Perelman L T, Itzkan I, Dasari R R and Feld M S 1997 Single molecule detection using surface-enhanced raman scattering (SERS) *Phys. Rev. Lett.* **78** 1667–70
- [12] Chen H-Y, Lin M-H, Wang C-Y, Chang Y-M and Gwo S 2015 Large-scale hot spot engineering for quantitative SERS at the single-molecule scale *J. Am. Chem. Soc.* **137** 13698–705
- [13] Wang D, Zhu W, Best M D, Camden J P and Crozier K B 2013 Wafer-scale metasurface for total power absorption, local field enhancement and single molecule Raman spectroscopy *Sci. Rep.* **3** 2867
- [14] Zhu K, Wang Z, Zong S, Liu Y, Yang K, Li N, Wang Z, Li L, Tang H and Cui Y 2020 Hydrophobic plasmonic nanoacorn array for a label-free and uniform sers-based biomolecular assay *ACS Appl. Mater. Interfaces* **12** 29917–27
- [15] Wang Q, Bai X, Zhang Y, Zhou Z, Guo M, Zhang J, Li C, Wang C and Chen S 2020 Layered assembly of silver nanocubes/polyelectrolyte/gold film as an efficient substrate for surface-enhanced raman scattering *ACS Appl. Nano Mater.* **3** 1934–41
- [16] Li J, Wuethrich A, Sina A A I, Cheng H-H, Wang Y, Behren A, Mainwaring P N and Trau M 2021 A digital single-molecule nanopillar SERS platform for predicting and monitoring immune toxicities in immunotherapy *Nat. Commun.* **12** 1087
- [17] Pillanagrovi J and Dutta-Gupta S 2022 Controlled assembly of gold nanoparticles in resonant gold nanoapertures for SERS applications *Nanotechnology* **33** 485301
- [18] Kubo W and Fujikawa S 2011 Au double nanopillars with nanogap for plasmonic sensor *Nano Lett.* **11** 8–15
- [19] Kang M, Park S-G and Jeong K-H 2015 Repeated solid-state dewetting of thin gold films for nanogap-rich plasmonic nanoislands *Sci. Rep.* **5** 14790
- [20] Dong Z et al 2015 Second-harmonic generation from sub-5 nm gaps by directed self-assembly of nanoparticles onto template-stripped gold substrates *Nano Lett.* **15** 5976–81
- [21] Siegfried T, Ekinci Y, Martin O J F and Sigg H 2013 Gap plasmons and near-field enhancement in closely packed sub-10 nm gap resonators *Nano Lett.* **13** 5449–53
- [22] Lopez G A, Estevez M-C, Soler M and Lechuga L M 2017 Recent advances in nanoplasmonic biosensors: applications and lab-on-a-chip integration *Nanophotonics* **6** 123–36
- [23] Xavier J, Vincent S, Meder F and Vollmer F 2018 Advances in optoplasmonic sensors—combining optical nano/microcavities and photonic crystals with plasmonic nanostructures and nanoparticles *Nanophotonics* **7** 1–38
- [24] Wang A and Kong X 2015 Review of recent progress of plasmonic materials and nano-structures for surface-enhanced raman scattering *Materials* **8** 3024–52
- [25] Kamińska A, Winkler K, Kowalska A, Witkowska E, Szymborski T, Janeczek A and Waluk J 2017 SERS-based immunoassay in a microfluidic system for the multiplexed recognition of interleukins from blood plasma: towards picogram detection *Sci. Rep.* **7** 10656
- [26] Ren X, Nam W, Ghassemi P, Strobl J S, Kim I, Zhou W and Agah M 2020 Scalable nanolaminated SERS multiwell cell culture assay *Microsyst. Nanoeng.* **6** 47
- [27] Vo-Dinh T, Wang H-N and Scaffidi J 2009 Plasmonic nanoprobe for SERS biosensing and bioimaging *J. Biophoton.* **3** 89–102
- [28] Schütz M, Steinigeweg D, Salehi M, Kömpe K and Schlücker S 2011 Hydrophilically stabilized gold nanostars as SERS labels for tissue imaging of the tumor suppressor p63 by immuno-SERS microscopy *Chem. Commun.* **47** 4216–8
- [29] Li Z, Huang X and Lu G 2020 Recent developments of flexible and transparent SERS substrates *J. Mater. Chem. C* **8** 3956–69
- [30] Wei H, Hossein Abtahi S M and Vikesland P J 2015 Plasmonic colorimetric and SERS sensors for environmental analysis *Environ. Sci. Nano* **2** 120–35
- [31] Oriňáková R, Škantárová L, Oriňák A, Demko J, Kupková M and Andersson J T 2013 Electrochemical deposition of SERS active nanostructured silver films *Int. J. Electrochem. Sci.* **8** 80–99 (<https://citeseerx.ist.psu.edu/document?repid=rep1&type=pdf&doi=b92113a22c81970517397c9044ead026244ab66e>)
- [32] Ivleva N P, Wagner M, Szkola A, Horn H, Niessner R and Haisch C 2010 Label-Free in Situ SERS Imaging of Biofilms *J. Phys. Chem. B* **114** 10184–94
- [33] Stokes D L and Vo-Dinh T 2000 Development of an integrated single-fiber SERS sensor *Sensors Actuators B* **69** 28–36

- [34] Yang K, Zong S, Zhang Y, Qian Z, Liu Y, Zhu K, Li L, Li N, Wang Z and Cui Y 2020 Array-assisted sers microfluidic chips for highly sensitive and multiplex gas sensing *ACS Appl. Mater. Interfaces* **12** 1395–403
- [35] Wu X, Luo L, Yang S, Ma X, Li Y, Dong C, Tian Y, Zhang L, Shen Z and Wu A 2015 Improved SERS nanoparticles for direct detection of circulating tumor cells in the blood *ACS Appl. Mater. Interfaces* **7** 9965–71
- [36] Cong L, Wang J, Li X, Tian Y, Xu S, Liang C, Xu W, Wang W and Xu S 2022 Microfluidic droplet-SERS platform for single-cell cytokine analysis via a cell surface bioconjugation strategy *Anal. Chem.* **94** 10375–83
- [37] Abu Hatab N A, Oran J M and Sepaniak M J 2008 Surface-enhanced raman spectroscopy substrates created via electron beam lithography and nanotransfer printing *ACS Nano* **2** 377–85
- [38] Bahramipناه M, Dutta-Gupta S, Abasahl B and Martin O J F 2015 Cavity-coupled plasmonic device with enhanced sensitivity and figure-of-merit *ACS Nano* **9** 7621–33
- [39] Wang X, Zhu J, Wu Y, Xu Y, Su Y, Zhang L, Qi Y, Wen X and Yang H 2020 Hybrid surface plasmon effect and SERS characterization in a heterogeneous composite structure of Au nano-array and Ag film *Res. Phys.* **17** 103175
- [40] Yildiz B C, Habib M, Rashed A R and Caglayan H 2019 Hybridized plasmon modes in a system of metal thin film-nanodisk array *J. Appl. Phys.* **126** 113104
- [41] Ameling R, Langguth L, Hentschel M, Mesch M, Braun P V and Giessen H 2010 Cavity-enhanced localized plasmon resonance sensing *Appl. Phys. Lett.* **97** 253116
- [42] Chu Y and Crozier K B 2009 Experimental study of the interaction between localized and propagating surface plasmons *Opt. Lett.* **34** 244–6
- [43] Yan Z, Du W, Tu L, Gu P, Huang Z, Zhan P, Liu F and Wang Z 2015 A facile high-performance SERS substrate based on broadband near-perfect optical absorption *J. Raman Spectrosc.* **46** 795–801
- [44] Bagheri S, Strohfeldt N, Sterl F, Berrier A, Tittl A and Giessen H 2016 Large-area low-cost plasmonic perfect absorber chemical sensor fabricated by laser interference lithography *ACS Sens.* **1** 1148–54
- [45] Ye S, Wang H, Wang H, Chang L, Zhang J and Yang B 2017 Rationally designed particle-in-aperture hybrid arrays as large-scale, highly reproducible SERS substrates *J. Mater. Chem. C* **5** 11631–9
- [46] Wei H, Håkanson U, Yang Z, Höök F and Xu H 2008 Individual nanometer hole-particle pairs for surface-enhanced raman scattering *Small* **4** 1296–300
- [47] Mubeen S, Zhang S, Kim N, Lee S, Krämer S, Xu H and Moskovits M 2012 Plasmonic properties of gold nanoparticles separated from a gold mirror by an ultrathin oxide *Nano Lett.* **12** 2088–94
- [48] Cesario J, Quidant R, Badenes G and Enoch S 2005 Electromagnetic coupling between a metal nanoparticle grating and a metallic surface *Opt. Lett.* **30** 3404–6
- [49] Liu N, Mesch M, Weiss T, Hentschel M and Giessen H 2010 Infrared perfect absorber and its application as plasmonic sensor *Nano Lett.* **10** 2342–8
- [50] Anam M K and Choi S 2020 Perfect absorption efficiency circular nanodisk array integrated with a reactive impedance surface with high field enhancement *Nanomaterials* **10** 258
- [51] Chanda D, Shigeta K, Truong T, Lui E, Mihi A, Schulmerich M, Braun P V, Bhargava R and Rogers J A 2011 Coupling of plasmonic and optical cavity modes in quasi-three-dimensional plasmonic crystals *Nat. Commun.* **2** 479
- [52] Ng C, Wesemann L, Panchenko E, Song J, Davis T J, Roberts A and Gómez D E 2019 Plasmonic near-complete optical absorption and its applications *Adv. Opt. Mater.* **7** 1801660
- [53] Lévêque G and Martin O J F 2006 Tunable composite nanoparticle for plasmonics *Opt. Lett.* **31** 2750–2
- [54] Nicolas R, Lévêque G, Marae-Djouada J, Montay G, Madi Y, Plain J, Herro Z, Kazan M, Adam P M and Maurer T 2015 Plasmonic mode interferences and Fano resonances in metal-insulator-metal nanostructured interface *Sci. Rep.* **5** 14419
- [55] Chu Y, Banaee M G and Crozier K B 2010 Double-resonance plasmon substrates for surface-enhanced raman scattering with enhancement at excitation and stokes frequencies *ACS Nano* **4** 2804–10
- [56] Johnson P B and Christy R W 1972 Optical constants of the noble metals *Phys. Rev. B* **6** 4370–9
- [57] König T A F, Ledin P A, Kerszulis J, Mahmoud M A, El-Sayed M A, Reynolds J R and Tsukruk V V 2014 Electrically tunable plasmonic behavior of nanocube-polymer nanomaterials induced by a redox-active electrochromic polymer *ACS Nano* **8** 6182–92
- [58] Xia H, Xiahou Y, Zhang P, Ding W and Wang D 2016 Revitalizing the frens method to synthesize uniform, quasi-spherical gold nanoparticles with deliberately regulated sizes from 2 to 330 nm *Langmuir* **32** 5870–80
- [59] Miller M D and Bruening M L 2005 Correlation of the swelling and permeability of polyelectrolyte multilayer films *Chem. Mater.* **17** 5375–81
- [60] Jeppesen C, Mortensen N A and Kristensen A 2010 The effect of Ti and ITO adhesion layers on gold split-ring resonators *Appl. Phys. Lett.* **97** 263103
- [61] Kim Y J, Jin S B, Kim S I, Choi Y S, Choi I S and Han J G 2010 Effect of oxygen flow rate on ITO thin films deposited by facing targets sputtering *Thin Solid Films* **518** 6241–4